

Experiments on turbulence beneath a free surface in a stationary field generated by a Crump weir: turbulence structure and correlation with the free surface

Sandro Longo

Received: 27 January 2010/Revised: 18 June 2010/Accepted: 21 June 2010/Published online: 3 July 2010
© Springer-Verlag 2010

Abstract This paper is a companion paper to a study devoted to the analysis of experimental instantaneous fluid levels and three-component fluid velocity measurements in a stationary flow field generated by a Crump weir in a laboratory flume, using an ultrasonic distance sensor and a three-probe arrangement of an ultrasonic Doppler velocity profiler (UVP) (Longo in Exp Fluids, doi:10.1007/s00348-010-0881-5, 2010). Whereas Longo (Exp Fluids, doi:10.1007/s00348-010-0881-5, 2010) deals with a general overview of the problem, the description of the experiments and the analysis of the free surface statistics and relevant scales, the present manuscript is devoted to a detailed analysis of the turbulence and the correlation with the free surface. The data are elaborated by obtaining the macroturbulence Reynolds tensor, using conditional averages based on free surface–fluctuation statistics. We also compute the two-point correlations of fluid velocity, the micro-scale and the integral scale, the correlation between free surface and the turbulence beneath. A free surface–boundary layer was detected having a thickness proportional to the root mean square of the free surface–height series and with a velocity scale that correlates well with the free surface–elevation time gradient. Most of the relevant state variables, such as the mean velocity and Reynolds stress components, collapse to a single curve if scaled appropriately. There are many indicators that a specific regime occurs that has an optimal tuning between the free surface and turbulence. In this regime, the length scales are considered as an indicator.

Abbreviations

$\langle \dots \rangle$	Space average operator
$\overline{\dots}$	Time average operator
$\widetilde{\dots}$	Phasic average operator
$E\{\dots\}$	Ensemble average operator
κ	Turbulent kinetic energy
Λ_{ij}	Integral length scale in the i -direction on using the j -component fluctuating velocity
λ_{ij}	Taylor length scale in the i -direction on using the j -component fluctuating velocity
ρ	Mass density
ν	Kinematic fluid viscosity
ω_i	Vorticity component
Ψ	Coherence
χ	Non-dimensional two-point correlation
τ	Bottom stress
ξ, ζ	Spatial coordinate
b_{ij}	Tensor of the 2nd order
c	Celerity of propagation of ultrasound
Fr, Fr_s	Froude number, based of free surface scales
H, H_{rms}	Wave height, root mean square wave height
$H_{1/3}$	Highest one-third wave
I_1, I_2, I_3	Invariants
k	Coefficient
L	Length scale
P_{ab}	Power cross-spectral density between the variables a and b
q	Velocity scale
$R_{u_j u_j}$	Correlation function
Re, Re_s	Reynolds number, based on surface scales

S. Longo (✉)
Department of Civil Engineering, University of Parma,
Viale G.P. Usberti, 181/A, 43100 Parma, Italy
e-mail: sandro.longo@unipr.it

t	Time
TKE	Turbulent kinetic energy
US	Ultrasound
UVP	Ultrasonic doppler velocity Profiler
u, v, w	Streamwise, spanwise, vertical fluid velocity
u', v', w'	Streamwise, spanwise, vertical fluctuating fluid velocity
$u'_{\text{rms}}, v'_{\text{rms}}, w'_{\text{rms}}$	Streamwise, spanwise, vertical root mean square value of the fluctuating fluid velocity
u_s	Velocity scale
We_s	Weber number, based on surface scales
x, y, z, x_i	Spatial co-ordinates
\mathbf{x}, \mathbf{s}	Space vector
z_s	Instantaneous level of the free surface

1 Introduction

The importance of the analysis of turbulence in many environmental and industrial flows relies on the high efficiency of turbulence exchange (of momentum, thermal energy, chemical components) with respect to molecular diffusion exchange. The early model of mass transfer at the interface was based on the role of the surface film. Higbie (1935) introduced a ‘penetration’ model to evaluate the parameters of the transfer processes near the free surface, assumed as a diffusion process. Dankwerts (1951) removed the conventional picture of a mass transfer between fluid and gas controlled by the liquid film; instead, a surface-renewal mechanism, controlled by turbulence, was postulated as the most important responsible of the process, affecting the exchange coefficients as used in the mass transfer equations of chemicals.

After conceptual models, the necessity to correlate the coefficients of the transfer equation with some measurable characteristic of the flow field near the interface was soon evident. A first theoretical analysis by Sirkar and Hanratty (1970), devoted to turbulent exchange near a wall, was later extended by McCready et al. (1986) to a slip-free interface in a cocurrent current air–water flow, with the aim of finding a relation between the transfer coefficients at the interface and the spectrum of the gradient of vertical velocity fluctuations. With a similar aim, Tamburrino and Gulliver (2002) fitted a linear model with experimental data obtained at the free surface in a moving-bed flume.

Clearly, turbulence is considered a major factor affecting interfacial phenomena. The classical analysis of turbulence is usually integrated by the description of turbulent fields in terms of their coherent structure. The coherent

structures are interesting as they play a major role in transport phenomena in the flow field and at an interface. Due to the presence of bursting phenomena, surface-renewal motions in the interfacial region below a gas (air)–liquid (water) interface take place.

Komori et al. (1989), using flume experiments, demonstrated that the frequency of surface renewal is determined by the outer-flow variables and the Reynolds number, with mass transfer across the interface dominated by large-scale eddies and a mass transport coefficient proportional to the square root of the surface-renewal frequency. In almost all physical situations, coherent structures (such as eddies impinging the free surface) generate waves. The generation of waves upon the water surface and the interaction with the fluid turbulence have been analysed by Teixeira and Belcher (submitted), who followed the paper by Phillips (1957). Phillips suggested a resonance of the turbulent pressure fluctuations in the air with the interface, resulting in the generation of waves. Among these waves, those matching the velocity of advection of the pressure fluctuations with their phase speed grew most rapidly. Teixeira and Belcher (submitted) claim that pressure fluctuations in the water phase can also generate free surface waves, and that these can be much more energetic than waves generated by pressure fluctuations in the air. Phillips’ theory has received only partial validation, as it requires measurements of the pressure field, and this is beyond present capabilities.

The experimental study of the interaction between turbulence and free surfaces has taken advantage of several “turbulent generators”, which are described briefly herein.

The most common experimental apparatus is a constant-depth, two-dimensional open channel, with turbulence generated near the bottom and largely invariant in the streamwise direction, at least far from the inlet and outlet. Starting from the inlet of the channel, a boundary layer develops and then occupies the entire flow domain, up to the free surface. Bursting at the bottom favours eddy movement that can reach the free surface and provide most of the ‘renewal’ of the surface (Nakagawa and Nezu 1977; Komori et al. 1989). The free surface suppresses vertical fluctuations and enhances tangential fluctuations, and at small Froude numbers, the surface tension can be strong enough to prevent surface waves.

A moving-bed flume (a flume with a belt as a moving bottom) has been used to study the structure of the outer-flow region and of the large streamwise vortices creating upwelling and downwelling motions at the free surface (Tamburrino and Gulliver 1999).

Grid-stirred tank experiments with a free surface (Brumley and Jirka 1983) have many attributes of channel flows in that the source of turbulence can be far from the free surface (to avoid coupling between the grid generation

mechanism and the free surface response). They have the advantages that the turbulence field is homogeneous and isotropic in the horizontal plane and nearly isotropic in the vertical plane.

Towed hydrofoils submerged near the free surface in an open channel have been used to distort the free surface and induce the breaking of the interface (Battjes and Sakai 1981). The hydrofoils generate a self-preserving turbulent wake flow that can be controlled, and the generated turbulence has a maximum near the toe of the breaking surface, before decaying downward and downstream.

In the present experiments, instantaneous fluid levels and three-component fluid velocity measurements were made in a stationary flow field generated by a Crump weir in a laboratory flume using an ultrasonic distance sensor and a three-probe arrangement of an ultrasonic Doppler velocity profiler. Several tests were carried out with increasing Froude number. The flow field in the measurement section is controlled by a spilling-type breaker generated on a steady current by the Crump weir. The weak roller downstream of the weir triggers the turbulence, which is generated near the free surface. The turbulence is then convected and dissipated downstream and downwards, with many characteristics similar to those of a turbulent wake. A downstream variation of the turbulence is inferred, possibly with a change of the structure of the turbulence but with a presumed self-similarity, at least up to the downstream section in which the interaction with the boundary layer of the bottom has not yet occurred. The details of the experimental setup and some preliminary analyses of the data are reported in Longo (2010).

This paper is organised as follows: Sect. 2 is devoted to describing and discussing turbulence and turbulence structure. Section 3 analyses the two-point velocity correlation, the macro- and microscales and the coherence between free surface elevation and the turbulence beneath it. The conclusions are outlined in the final section.

2 Turbulence characteristics

2.1 Turbulent velocity components

The preliminary analyses of the data presented in Longo (2010) have revealed the existence of a length scale H_{rms} and a velocity scale u_s in the free surface–boundary layer (H_{rms} is the root mean square of the free surface–wave heights as detected on using a zero(up) crossing technique, $u_s = \sqrt{(dz_s/dt)^2}$ is the root mean square value of the free surface–vertical velocity, where z_s is the instantaneous vertical position of the free surface). Beneath the free

surface and for limited free surface fluctuations, turbulence is non-isotropic and two-dimensional, with the horizontal and vertical components strongly damped approaching the free surface. The energy related to vertical component fluctuations increases with depth and reaches a constant value at $z \sim -4$ mm (Fig. 1), where the energy contributions of the other two components reach their maximum values. The test with limited free surface fluctuations is the nearest to the physical conditions studied by Calmet and Magnaudet (2003) and Swean et al. (1991), and these results can be compared. According to Swean et al. (1991) and Calmet and Magnaudet (2003), the turbulence entering the region near the free surface tends to be more isotropic as the Reynolds number increases (the Reynolds number is computed on the base of the wall length scale). There are two mechanisms responsible for the redistribution of turbulent kinetic energy (TKE). The first is the classical pressure-strain term that acts to reduce the anisotropy, at least far from the boundary. The same pressure-strain term acts to increase the anisotropy near the boundaries (and hence near the free surface), transferring energy from the vertical fluctuations towards the tangential fluctuations. The two mechanisms act to increase the spanwise velocity fluctuations, but the intensities of their effects depend on the structure of the turbulence reaching from the bottom to the free surface. If this turbulence is almost isotropic (at large Reynolds numbers), the pressure–strain correlation simply increases the spanwise component. If the turbulence is far from isotropic, the streamwise component is strongest, and the pressure strain acts to reduce the streamwise component and increase the other two components. However, very near the free surface, the ultimate enhancement

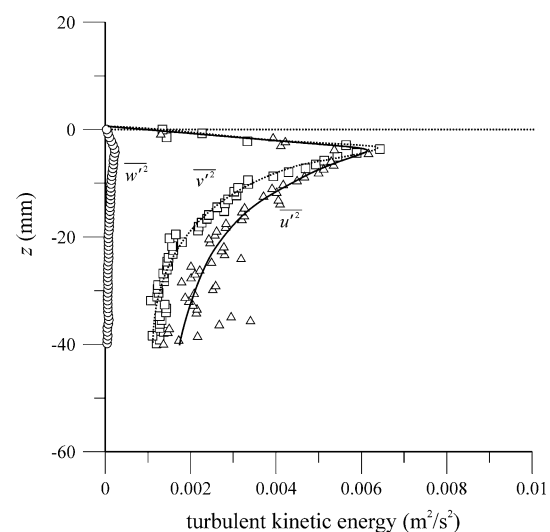


Fig. 1 Profiles of the turbulence fluctuation of velocity, x , y and z -components. Test No 64, $H_{\text{rms}} = 0.77$ mm

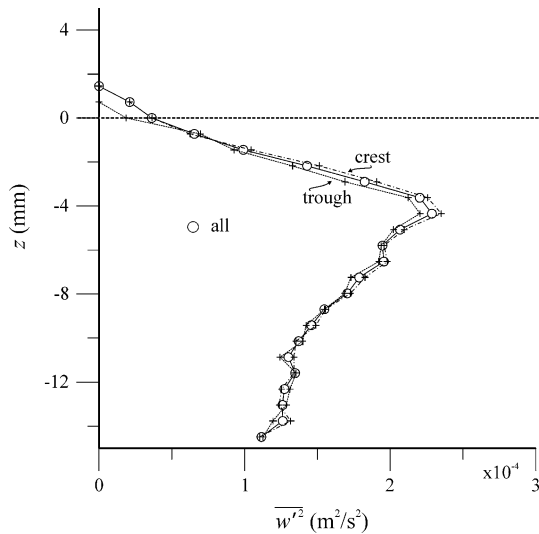


Fig. 2 Profiles of the turbulence fluctuation of vertical velocity, computed for restricted statistics of free surface elevation. The *dashed line* refers to the restricted statistics considering only the troughs and (*dot-dashed*) the crests. Test No 64, $H_{rms} = 0.77$ mm

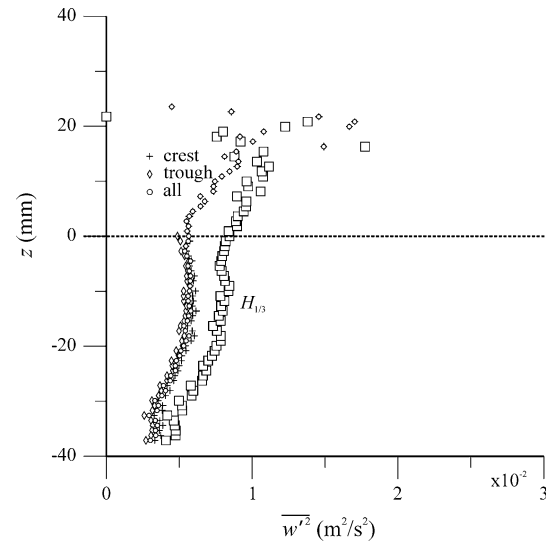


Fig. 3 Profiles of the turbulence fluctuation of vertical velocity, computed for restricted statistics of free surface elevation. Test No 66, $H_{rms} = 12.09$ mm

is for the spanwise component. In the present experiments, for the lowest H_{rms} , the streamwise and spanwise components have similar profiles, with a maximum at the apparent lower limit of the free surface–boundary layer. The vertical fluctuation is nearly zero at the interface, and the turbulent kinetic energy (essentially due to the two horizontal components) increases. The experimental results are not affected by the phasic average, considering that at low H_{rms} , the phasic and time average are quite coincident. The scenario is different from that depicted by Swean et al. 1991 and Calmet and Magnaudet, due to the different source of the turbulence. Assuming that most turbulent energy production is due to the term $-\overline{u'w'}\left(\frac{\partial u}{\partial z}\right)$, and observing the Reynolds stress and the shear velocity profiles, we can guess that the energy source is located in the lower part of the free surface–boundary layer, at least for the test with the lowest value of H_{rms} . The vertical fluctuation increases with H_{rms} and is generally smaller than the other two components in all tests. Its profile in the vertical direction is strongly dampened for small values of H_{rms} . In Figs. 2, 3, this profile is shown for all data, for the crests and for the troughs, referring to the test of the minimum and maximum values of H_{rms} . The trends of the profiles are quite similar, even though the fluctuations are higher during the crests than the troughs. The level of turbulence is generally computed to be higher for the highest free surface fluctuations. A similar behaviour can be observed for all the data sets and for the other two components of fluctuating velocity. In particular, the ratio of energy is shown in Fig. 4 for the test with $H_{rms} = 12.09$ mm, including the subset that relate to the

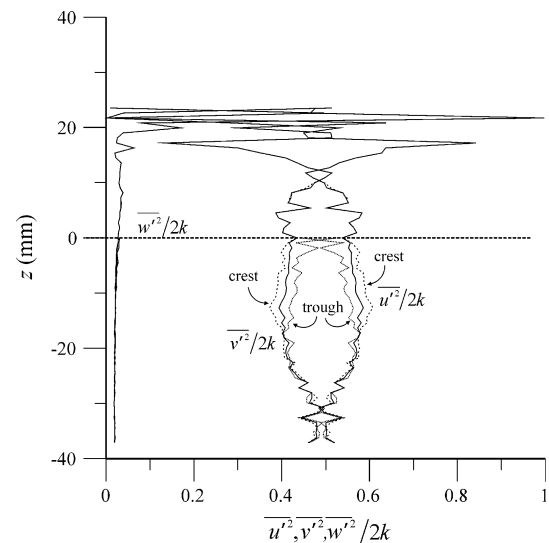


Fig. 4 Turbulence energy ratio for the whole data set and for restricted statistics: *dashed lines* for the crests, *dotted lines* for the troughs. Test No 66, $H_{rms} = 12.09$ mm

crests and troughs only. The interpretation of this data is postponed to the section where the structure of turbulence is analysed. The non-dimensional turbulence kinetic energy is shown in Figs. 5, 6, 7, 8. The data collapse fairly well in the boundary layer and confirm that our choice of scales appears suitable for all tests in the region between $+2H_{rms}$ and $-H_{rms}$, except for the tests with the smallest H_{rms} . In fact, in the presence of small free surface fluctuations, the length scale is presumably better related to fluid viscosity. For turbulence generated at the bottom, the velocity scale

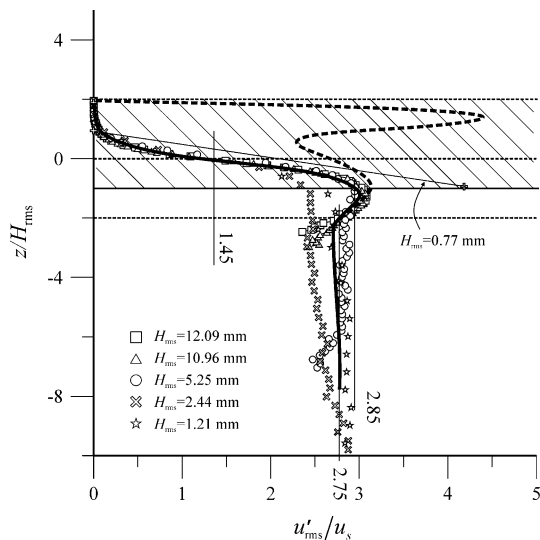


Fig. 5 Non-dimensional kinetic energy, streamwise component, time average (*bold line and symbols*) and phasic average (*dashed line*). The *dashed area* is the inner region

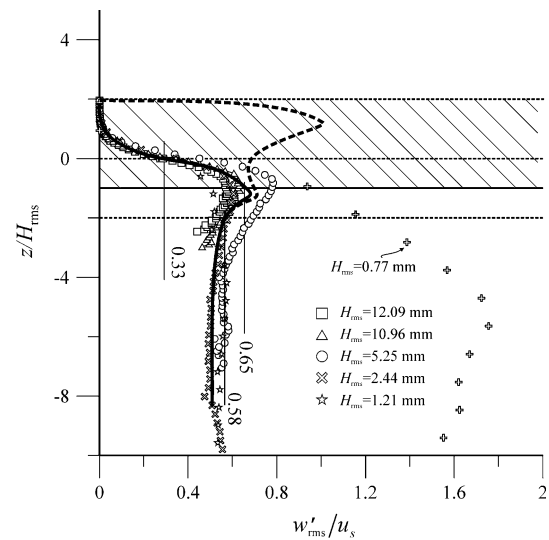


Fig. 7 Non-dimensional kinetic energy, vertical component, time average (*bold line and symbols*) and phasic average (*dashed line*). The *dashed area* is the inner region

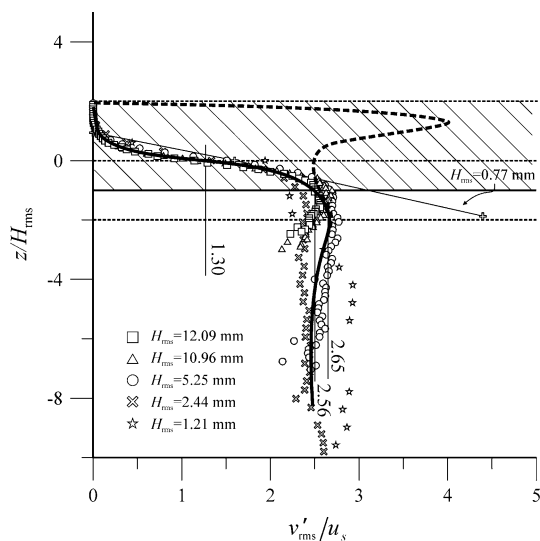


Fig. 6 Non-dimensional kinetic energy, spanwise component, time average (*bold line and symbols*) and phasic average (*dashed line*). The *dashed area* is the inner region

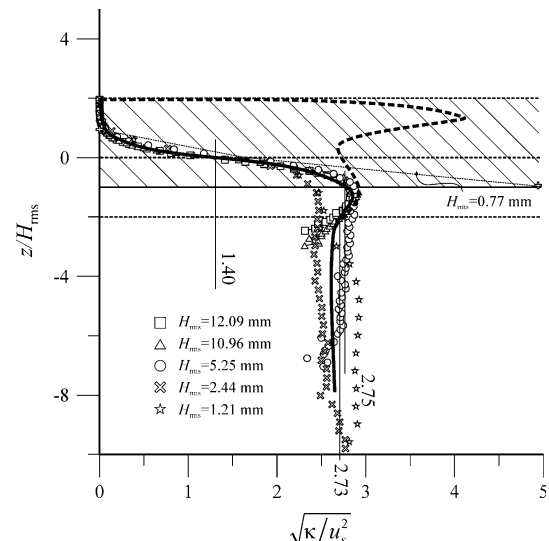


Fig. 8 Non-dimensional kinetic energy, time average (*bold line and symbols*) and phasic average (*dashed line*). The *dashed area* is the inner region

near the free surface is the friction velocity and the length scale is v/u_* , except for vorticity and related quantities, which scale with the Taylor length microscale (Calmet and Magnaudet 2003). However, in the present experiments, for an almost flat free surface, we can infer that the length scale is v/u_s . The assumption of u_s as the proper scale also at low values of H_{rms} is consistent with the assumed position of the source of turbulence near the free surface. This cannot be interpreted as the fact that turbulence is generated by the displacements of the free surface or that the surface is mostly deformed by eddies generated

elsewhere, but only that the two phenomena are intimately correlated. The coherence analysis in Sect. 3 gives more information on this point.

In some cases, it is possible to formulate a hypothesis regarding the structure of the turbulence (Nezu and Nakagawa 1993), thereby obtaining some simple theoretical profiles of the fluctuating components. Due to the complexity of the flow field near the experimental interface in the present tests, a hypothesis on the structure of the turbulence tends to complicate semi-theoretical relations, making empirical formulae more useful.

The best fit of the time averages in the domain $[-H_{rms}, H_{rms}]$ is obtained using the functions:

$$\begin{aligned}
 u'_{rms}/u_s &= 1.45 \left[1 - \operatorname{erf} \left(1.55 \frac{z}{H_{rms}} \right) \right], & R^2 &= 0.98 \\
 v'_{rms}/u_s &= 1.30 \left[1 - \operatorname{erf} \left(1.55 \frac{z}{H_{rms}} \right) \right], & R^2 &= 0.98 \\
 w'_{rms}/u_s &= 0.33 \left[1 - \operatorname{erf} \left(1.52 \frac{z}{H_{rms}} \right) \right], & R^2 &= 0.94 \\
 \sqrt{\kappa/u_s^2} &= 1.40 \left[1 - \operatorname{erf} \left(1.55 \frac{z}{H_{rms}} \right) \right], & R^2 &= 0.98
 \end{aligned}
 \tag{1}$$

In these equations, $\kappa = (\overline{u'^2} + \overline{v'^2} + \overline{w'^2})/2$ is the turbulent kinetic energy (TKE). The shape of these functions is independent of the Reynolds and Froude numbers, even though some discrepancies are observed for the two tests at lower Froude numbers. These functions are monotonic, as expected due to the progressive reduction in the concentration of the fluids. Observing the phasic average profiles, an evident spike is present just near the expected maximum level reached by the water at least once during the tests. Due to the scatter of the data (because the number of measurements is fast decreasing in the vertical), no general conclusions can be drawn, and an extrapolation to the surface also cannot be made with confidence. Nevertheless, the presence of a ‘bulge’ in the horizontal velocity fluctuations near the surface has also been reported in Brumley and Jirka (1983) using a grid-generated turbulence.

The estimated values of turbulence intensities at $z = 0$ and $z = \pm H_{rms}$ are reported in Table 1.

The phasic maximum level of turbulence is in the crest and is equal to $\sqrt{\kappa/u_s^2} \simeq 4.0$. Below the mean water level, turbulence increases again (phasic average), while in the outer region ($z < -2H_{rms}$), it is controlled by different features and scales of the flow field.

From Eq. 1, one can also obtain the ratios of the redistribution of the turbulent energy. Despite the high value of the coefficient of determination, in the limits of the confidence band, we can assume that the parameter of the $\operatorname{erf}(\dots)$ function is equal to 1.55 for all three components (including the vertical component), yielding constant uniform ratios equal to $\overline{u'^2}/2k = 0.54$, $\overline{v'^2}/2k = 0.43$, $\overline{w'^2}/2k = 0.03$, which confirms the relation $u'_{rms} > v'_{rms} \gg w'_{rms}$. For comparison, the ratios measured in the intermediate region of an open channel are $\overline{u'^2}/2k =$

Table 1 Estimated values of turbulence at some specific levels

z/H_{rms}	u'_{rms}/u_s	v'_{rms}/u_s	w'_{rms}/u_s	$\sqrt{\kappa/u_s^2}$
+1	0.04	0.036	0.010	0.039
0	1.45	1.30	0.33	1.40
-1	2.85	2.56	0.65	2.75

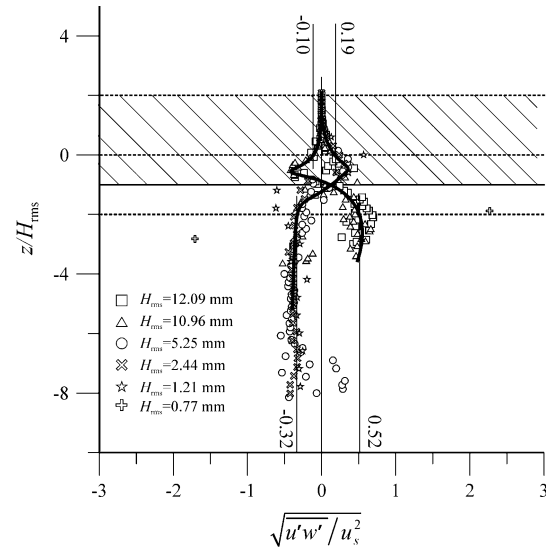


Fig. 9 Non-dimensional Reynolds stress $\overline{u'w'}$, time average

0.54 , $\overline{v'^2}/2k = 0.28$, $\overline{w'^2}/2k = 0.17$ (Nezu and Nakagawa 1993). In Fig. 9, the component $\overline{u'v'}$ (streamwise-vertical) of the Reynolds stress is shown. At the mean water level ($z = 0$), the momentum flux is low for the highest value of H_{rms} ($Fr > 0.30$) and is equal to $\overline{u'w'}|_{z=0} \simeq -0.01u_s^2$; lower values of H_{rms} yield $\overline{u'w'}|_{z=0} \simeq 0.04u_s^2$. The momentum flux is equivalent to a stress exerted by the layer above the mean water level on the domain beneath, and by adopting the usual definition of friction velocity, the stress can be expressed as $\tau = \rho u_*^2$, with a friction velocity equal to $u_* = 0.10u_s$ and $u_* = 0.19u_s$, for $Fr > 0.30$ and $Fr < 0.30$, respectively. In the first case ($Fr > 0.30$), the stress is positive and acts to accelerate the core of the flow field, and in the second case ($Fr < 0.30$), it is negative and acts to decelerate the core of the flow field. For $Fr < 0.30$, the stress acts as it would in the presence of a rigid wall, subtracting momentum from the flow field; at higher levels of fluctuation, the stress acts by generating a net positive momentum influx towards the flow field. A threshold is expected at zero tangential stress, which fixes the transition between the two different regimes. The different regimes can be interpreted as a consequence of the different correlations between the free surface fluctuations and velocity fluctuations that occur with different phase lags at different levels and at different Froude numbers. Essentially, at a high Froude number, the free surface fluctuations are quite active in generating vertical velocity fluctuations (sometimes also with microbreaking), which modify the general correlation pattern with the streamwise velocity fluctuations. The result is a tangential stress that changes sign as a function of the Froude number.

For all levels of $z = -H_{rms}$, the results are $\overline{u'w'}|_{z=-H_{rms}} \simeq 0$, and the zero tangential stress condition

usually imposed at the free surface can still be applied—but at the lower limit of the boundary free surface layer, almost independent of the value of H_{rms} .

At the interface with the outer region ($z = -2H_{rms}$), the momentum flux is equal to $\overline{u'w'}|_{z=-2H_{rms}} \cong -0.10u_s^2$ for $Fr < 0.30$ and $\overline{u'w'}|_{z=-2H_{rms}} \cong 0.27u_s^2$ for $Fr > 0.30$. The trend is similar if we look at the phasic average, showing a large data dispersion above the mean water level but an organised pattern immediately below the mean water level. As usual, the data from test No. 64 do not follow the general trend.

We use extensively the phasic and the time averages, and other different kinds of averages are available. It is important to highlight that generally speaking there is no more physics in a phasic than in a time or other kind of averages. There is simply a different point of view of the same process but care is necessary in evaluating the results.

2.2 The structure of turbulence in terms of the invariants

The imposition of kinematic and dynamic boundary conditions at the free surface makes turbulence anisotropic and generally increases the spanwise component (Shen et al. 1999). To quantify the degree of anisotropy in the flow, we used Lumley’s analysis (Lumley and Newman 1977). Given the tensor b_{ij} and defining the invariants as

$$\begin{aligned} I_1 &= b_{kk} \\ I_2 &= -\frac{1}{2}b_{ij}b_{ji} \\ I_3 &= \det(b_{ij}) \end{aligned} \tag{2}$$

(summation is implicit), the anisotropy invariant map can be obtained using some theoretical relationships for isotropic, axisymmetric, 1-component and 2-component turbulence (Simonsen and Krostad 2005):

$$\begin{aligned} I_2 = I_3 = 0 & \text{ isotropic} \\ -\frac{I_2}{3} = \left(\pm\frac{I_3}{2}\right)^{2/3} & \text{ axisymmetric} \\ I_3 = \frac{2}{27}, I_2 = -\frac{1}{3} & \text{ one-component} \\ I_3 = -\frac{1}{108}, I_2 = -\frac{1}{12} & \text{ two-component axisymmetric} \\ -I_2 = 3\left(\frac{1}{27} + I_3\right) & \text{ two-component} \end{aligned} \tag{3}$$

The results are shown in Fig. 10. Near the free surface (the first level with non-zero water concentration), the turbulence is almost one-dimensional at a high level of free surface fluctuations ($H_{rms} = 12.09$ mm) and then turns into a two-component object moving downward in the fluid domain, becoming disc-like axisymmetric, with a small

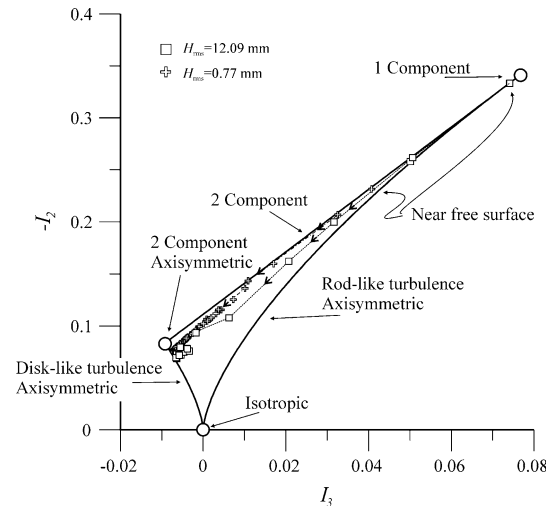


Fig. 10 Anisotropy invariant map in the Eulerian reference system for the two extreme tests. The arrows indicate the evolution of turbulence downward, with the first bullet at the free surface (the first level with a non-zero water concentration)

principal stress (along z) and two larger principal stresses (streamwise and spanwise). For the lowest free surface fluctuations ($H_{rms} = 0.77$ mm) near the free surface, the turbulence is essentially two-component in the x - y plane, then returns to being disc-like and axisymmetric. To check the effects of the modulation of the turbulence by the waves, we computed the invariants for the data set limited to (1) troughs and (2) crests for the test with $H_{rms} = 12.09$ mm, but we chose a Lagrangian reference with the origin at the instantaneous free surface level. The choice of the Lagrangian reference allows analysis of the turbulence while focusing on the eddies tied to the free surface. The vertical profile of the turbulence structure (Fig. 11) is similar during the two different phases, with an attitude to change from disc-like axisymmetric (i.e. two main eigenvalues of the same magnitude in the horizontal plane plus a third of smaller value in the vertical) to rod-like axisymmetric (i.e. two minor eigenvalues of the same magnitude plus a larger third one in the streamwise direction) more evident during the crests, at least in the first layer below the free surface. The evolution is a consequence of stretching in the streamwise direction, as depicted by Teixeira and Belcher (2002) for similar conditions: the effect of crests and troughs is to increase two of the three components of TKE, i.e. spanwise and streamwise during the crests versus spanwise and vertical during the troughs. The third component is generally non-zero but smaller than the other two components. In particular, Teixeira and Belcher used a simplified model in terms of vorticity to justify the observed behaviour, which should be a consequence of vortex stretching by the orbital motion of the waves. However, they predicted a

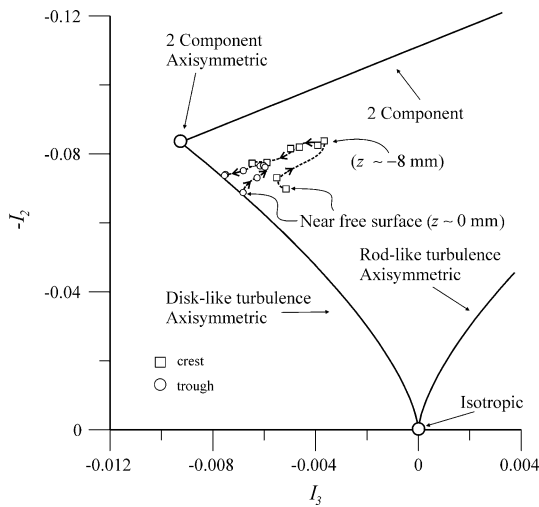


Fig. 11 Anisotropy invariant map in a Lagrangian reference system for the test with $H_{rms} = 12.09$ mm. Downward evolution during crests and during troughs

larger variation of the vertical component. Their prediction model is only partially applicable to the present experiments, which differ from their model because the waves play an active part in subtracting and releasing energy.

In addition, the analysis of the ratio of turbulent kinetic energy of the three components and the separation of crests and troughs (Fig. 4) confirms the scenario depicted earlier.

The variation of the relative content of TKE during the crests and troughs is approximately 10% for the two horizontal components and approximately 4% for the vertical component. It is also consistent with the results obtained by Britter et al. (1981) and by Thais and Magnaudet (1996).

3 The velocity two-point correlation

3.1 Spatial structure of turbulence

In addition to the invariant analysis reported in Sect. 2, the structure of turbulence can be analysed by examining the two-point correlation at different depths below the surface. The strong anisotropy suggests that the velocity two-point correlations are not homogeneous, and they have to be computed using the standard expression:

$$R_{u_i u_j}(\mathbf{x}_1, \mathbf{x}_2) = E\{u'_i(\mathbf{x}_1)u'_j(\mathbf{x}_2)\} \tag{4}$$

where E stands for the ensemble average. The summation notation is not implied for i and j . The inhomogeneity arises from a spreading of the flow into the non-turbulent fluid (the air at the interface). Due to the type of velocity

measurements performed, with a time lag in the velocity data at the two different gates, a correction for the proper evaluation of $R_{u_i u_j}$ is necessary and is obtained by developing a Taylor’s series, neglecting the higher-order contributions, as reported in the following.

Let us recall the definition for a homogeneous process:

$$R(t, \xi) = E\{u(t, x)u(t, x + \xi)\} \tag{5}$$

In our measurements, the velocities are sampled along a profile at time t but with a lag between two different gates. The time lag depends on the celerity of the ultrasound, c , and on the space lag:

$$\Delta t = k \frac{\xi}{c} \tag{6}$$

where k is a coefficient, ~ 2 . As a consequence, on using the measured data, we obtain the following function:

$$E\left\{u\left(t - k \frac{\xi}{c}, x\right)u(t, x + \xi)\right\} \tag{7}$$

which, developed in a Taylor’s series, becomes

$$E\left\{u\left(t - k \frac{\xi}{c}, x\right)u(t, x + \xi)\right\} = E\{u(t, x)u(t, x + \xi)\} - E\left\{\left(\frac{\partial u}{\partial t}\right)_{(t,x)} k \frac{\xi}{c} u(t, x + \xi)\right\} + O\left(k^2 \frac{\xi^2}{c^2}\right) \tag{8}$$

The corrected expression for the two-point correlation is

$$E\{u(t, x)u(t, x + \xi)\} = E\left\{u\left(t - k \frac{\xi}{c}, x\right)u(t, x + \xi)\right\} + E\left\{\left(\frac{\partial u}{\partial t}\right)_{(t,x)} k \frac{\xi}{c} u(t, x + \xi)\right\} + O\left(k^2 \frac{\xi^2}{c^2}\right) \tag{9}$$

and involves a two-point correlation between the velocity time gradient and the velocity.

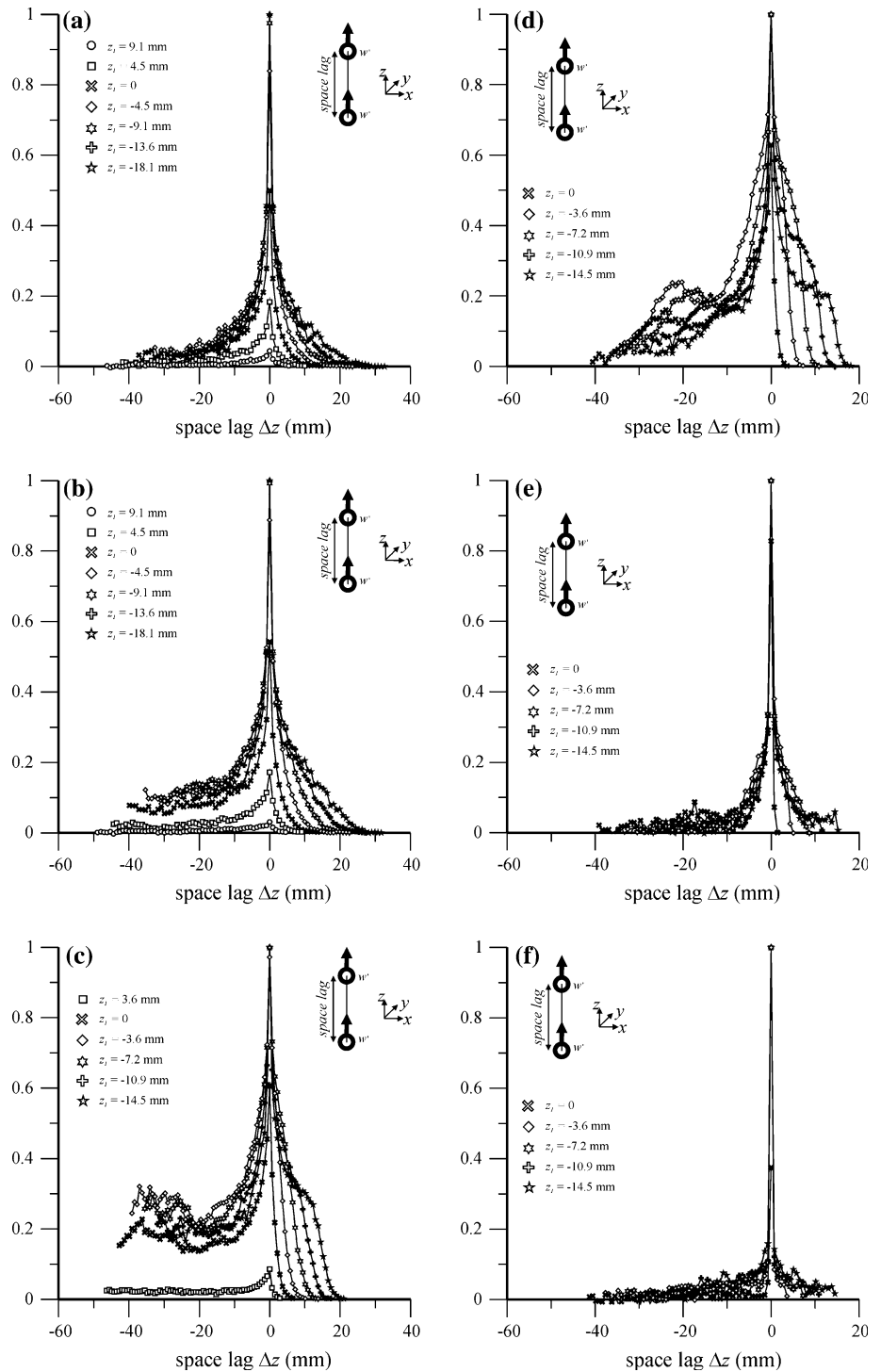
The extension to a non-homogeneous process is straightforward.

Here, only the properties of $R_{w'w'}$ in the vertical direction are described. Using the data, we can evaluate the function: $R_{w'w'}(z_1, z_2) = E\{w'(z_1)w'(z_2)\}$, normalised as

$$\begin{aligned} \chi(z_1, z_2) &= \frac{R_{w'w'}(z_1, z_2)}{\sqrt{R_{w'w'}(z_1, z_1)}\sqrt{R_{w'w'}(z_2, z_2)}} \\ &\equiv \frac{R_{w'w'}(z_1, z_2)}{w'_{rms}(z_1)w'_{rms}(z_2)} \end{aligned} \tag{10}$$

The two-point correlations for the vertical fluctuating velocity along the vertical direction, as computed at several depths, are shown in Fig. 12. The curves are non-symmetric, but a progressive evolution towards symmetry is observed for increasing values of H_{rms} . At intermediate values of H_{rms} , the shape is typical of turbulence with a wide spectrum of eddy size, while at low and high values, it turns to a shape that is typical of

Fig. 12 Vertical two-point non-dimensional correlation $\chi(z_1, z_1 + \Delta z)$: **a** test $H_{rms} = 12.09$ mm (test No 66); **b** test $H_{rms} = 10.96$ mm (test No 65); **c** test $H_{rms} = 5.25$ mm (test No 61); **d** test $H_{rms} = 2.44$ mm (test No 62); **e** test $H_{rms} = 1.21$ mm (test No 63); **f** test $H_{rms} = 0.77$ mm (test No 64)



turbulence with a single family of eddies. Notably, multiple eddies are present in the resonant condition (test Nos. 61 and 62). Eddy dynamics are characteristically largely independent of the characteristics of the forcing terms, under specific conditions, and are mainly related to the physical parameters of the system embedded in the relevant non-dimensional groups.

3.2 The macro- and microscales

The correlation functions can give additional information on the structure of turbulence on the macro- and microscales. The length macroscale Λ_{ij} , corresponding to the velocity component j in the direction x_i , is generally defined under isotropic homogeneous conditions as:

$$\Lambda_{ij} = \int_0^{\infty} R_{u_i u_j}(\Delta x_i) dx_i \quad (11)$$

In the flow field used here, both inhomogeneity and anisotropy occur. Therefore, considering the data set of the measurements, a better definition of the integral macroscale would be:

$$\Lambda_{zj}(z) = \frac{1}{2} \int_{-\infty}^{\infty} R_{u_j u_j}(z, \zeta) d\zeta \quad (12)$$

ζ represents the vertical coordinate. That is, the integral macroscale refers to autocorrelation in the vertical direction of one of the three velocity components and is also a function of the position in the vertical direction. In the following analysis, we assume for simplicity that the macroscales are representative of the three sizes of the vortices, even though this is not the case for strongly non-isotropic turbulence.

Figure 13 shows the vertical integral length scale profile (i.e. the vertical correlation length of the vertical velocity fluctuations). This varies slightly with a mean value of $\sim 1.5H_{\text{rms}}$ for tests with $Re_s < 300$. For higher values of Re_s , the mean value decays very rapidly ($\sim 0.5H_{\text{rms}}$ and $\sim 0.2H_{\text{rms}}$ for $Re_s = 1,132$ and $Re_s = 1,580$, respectively). Notably, the integral lengths scale well and the values of H_{rms} are of similar magnitude to the estimated thickness of the free surface–influenced layer (for limited Re_s values) and confirm the picture of turbulence that is generally controlled by the free surface parameters. The integral macroscale has a maximum at an intermediate fluctuation level ($H_{\text{rms}} = 5.25$ mm), and it can be

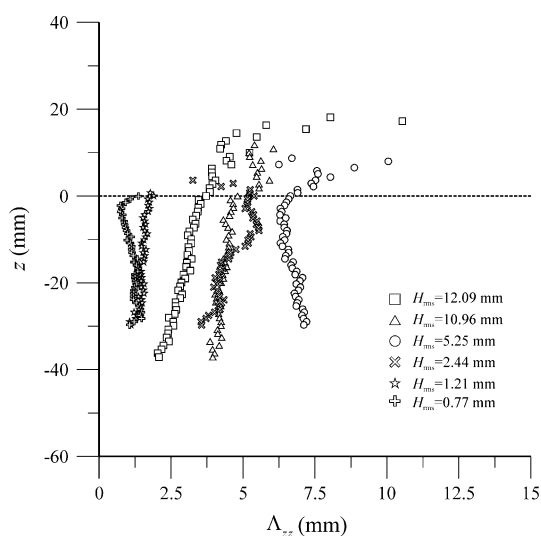


Fig. 13 Integral length scales in the vertical (vertical velocity)

addressed to an optimal tuning between the free surface oscillations and macrovortices. It then decays with respect to H_{rms} , suggesting that the organised interaction between the turbulence and the free surface is lost for increasing values of Re_s . This behaviour can be observed in the autocorrelation functions (see Fig. 12). At low values of Re_s (test Nos. 63 and 64), the length scale appears due to a single family of vortices that produce turbulence and dissipate most of it locally. The size of the vortices is related to the thickness of the free surface–influenced layer. At medium values of Re_s (tests 62 and 61), at least two families of vortices are present, with the larger generating a second spike in the autocorrelation function and the smaller (dissipative) near the origin of the time lag axis. The existence of the two families of vortices can be interpreted energetically as the growth, due to resonance phenomena, of the most efficient energy–extracting vortices; the smallest vortices dissipate the TKE locally. At high values of Re_s (test Nos. 65 and 66), resonance is lost and only the relatively small vortices persist; the convective transport of energy reduces the local dissipation of energy and limits the minimum size of the residual vortices.

A similar behaviour is observed in the two transverse integral scales, Λ_{zx} and Λ_{zy} (not shown), computed by the autocorrelation of the two horizontal velocity fluctuations in the vertical direction, but a general damping towards the mean water level is present even though it is much more evident at low H_{rms} . The two scales Λ_{zx} and Λ_{zy} are generally half the values of the integral length scale in the vertical direction. The reduction in the three vertical integral scales towards $z = 0$ at low H_{rms} is forecast by the ‘pancake’ model by Handler et al. (1993). This behaviour changes abruptly as soon as the stabilising effects of the tension surface and gravity disappear. For the tests with the highest value of H_{rms} , the scales for the vertical and streamwise velocities have a positive gradient near $z = 0$, showing that in this condition, the eddies are not merely compressed in the proximity of the interface but actively fill the fluid domain. In this last condition, the free surface is effective in favouring vortices of almost constant vertical size, increased streamwise size and damped spanwise size. In comparison, the integral length scales measured for a grid generating turbulence have a maximum in the bulk not far from the grid and decay towards the free surface (see Brumley and Jirka 1983). The damping effect of the free surface is much more evident than in the present experiments, due to the differences in the sources of turbulence and, in particular, to the different role of the free surface fluctuations.

A frequently used microscale is the Taylor microscale, defined as

$$\lambda_{ij}^2 = -2 \left| \frac{\partial^2 R_{u_j u_j}}{\partial x_i^2} \right|_{x_i=0} \quad (13)$$

This is not the smallest scale, but it is often assumed as the length scale where most dissipation takes place. The vertical microscale for the vertical velocity λ_{zz} is shown in Fig. 14. It is almost uniform in the vertical direction except at intermediate values of H_{rms} , as characterised by an increment in the free surface–boundary layer. The maximum values also occur at intermediate values of Fr_s . The two computed transverse Taylor microscales (λ_{zx} and λ_{zy} , not shown) are associated with the component of vorticity that lies parallel to the free surface (ω_x and ω_y). They are generally equal and uniform in the vertical direction, slightly damped in the free surface–boundary layer and generally smaller than λ_{zz} . At an intermediate Froude number ($Fr_s = 0.24$, $H_{rms} = 2.44$ mm), they are $\sim 30\%$ smaller than λ_{zz} . The microscale λ_{zz} increases by $\sim 30\%$ in the free surface–boundary layer. Considering that the vertical microscale can also be computed as:

$$\lambda_{zz}^2 = \frac{2w'^2}{(\partial w'/\partial z)^2} \quad (14)$$

and that the vertical fluctuation increases by less than 10%, the mean extensional strain $\partial w'_{rms}/\partial z$ has reduced by 40%.

To find the relation between the macroscale and the microscale, we checked the dependence of the Taylor microscale vs. the Reynolds number, expressed as:

$$Re_\Lambda = \frac{\Lambda_{zz} u_s}{\nu} \quad (15)$$

Assuming a local balance in isotropic turbulence, production equals dissipation and the relationship

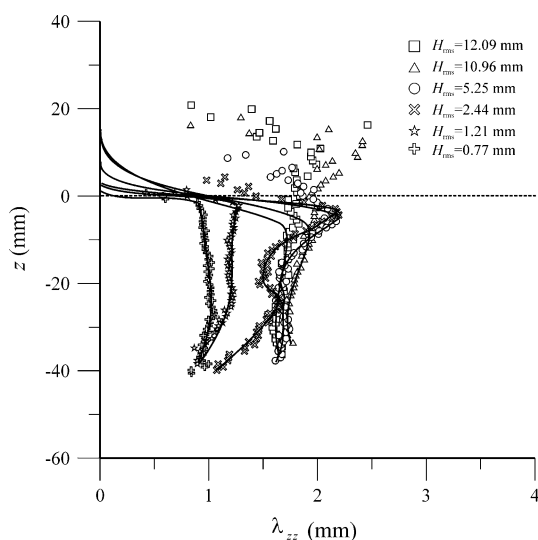


Fig. 14 Taylor vertical length scales for the vertical velocity, time average (*bold line*) and phasic average (*symbols*)

between the microscale and the macroscale is (Tennekes and Lumley 1972):

$$\frac{\lambda_{zz}}{\Lambda_{zz}} = \sqrt{\frac{15}{A}} Re_\Lambda^{-1/2} \quad (16)$$

being A a coefficient of order one. If the local energy balance is not satisfied, but still adopting the hypothesis of small-scale isotropy at large Reynolds numbers, a possible expression of this dependence is:

$$\frac{\lambda_{zz}}{\Lambda_{zz}} \propto Re_\Lambda^n \quad (17)$$

If we release the local energy balance and include the other terms in the turbulent energy budget, we realise that the pressure-work and mean transport of turbulent energy by turbulent motion are of scale u^3/Λ like the production term and hence do not modify the exponent $-1/2$ characteristic of the local equilibrium (they should simply modify the value of the constant). The transport by viscous stresses is of order $\nu u^2/\Lambda^2$, and this contribution would change the relation as $\lambda/\Lambda = \sqrt{15/(A'Re_\Lambda + B)}$ being A' and B two constants. A further contribution is the transport of turbulent energy by the mean motion, which depends on the specific flow field and which can modify the relationship. The diagrams for all tests are shown in Fig. 15. The Taylor microscale (and its ratio with the macroscale) decreases with the Reynolds number much faster than it generally does in the case of local energy balance, except for the test with $H_{rms} = 1.21$ mm. For this test, the best fitting has equation $\lambda/\Lambda = 5.25 Re_\Lambda^{-0.538}$ and the computed value of the coefficient is $A = 0.54$. Considering that the Taylor microscale is adopted as the scale of dissipation, the reduction of its value to balance the energy production at a rate faster than the local equilibrium

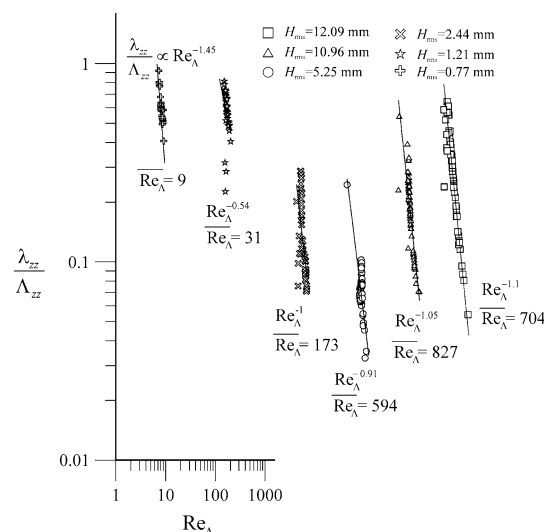


Fig. 15 Relation between microscale and Reynolds number

hypothesis would suggest that a large influx of energy is present due to either transfer from other regions of the flow field or to the free surface fluctuations acting as a source. The sensitivity is much exaggerated for an almost flat free surface (i.e. low H_{rms}), which has an exponent of Re_Λ equal to -1.45 . However, this is not generally valid, due to the dominance of other scales for an almost flat free surface. The local equilibrium is almost satisfied for the test when $H_{rms} = 1.21$, and then the exponent of the Re_Λ number almost equals -1 at high values of H_{rms} . Note that these considerations are based on a partial view of the global phenomenon, as we are considering essentially only the turbulence dynamics in the vertical direction.

Evaluation of the kinetic turbulence energy and relevant length scales allows the categorisation of the flow according to tentative descriptions of the flow regimes reported by Brocchini and Peregrine (2001). In their description, the authors adopt a velocity scale q that is related to TKE, with $\kappa = \frac{1}{2}q^2$, and a length scale L that is related to the dominant surface features. While we have a close estimation of q , the length scale L shall be approximated by Λ_{zz} . The diagram is shown in Fig. 16; the output of the present tests are plotted as ellipses with vertical axes ranging between the TKE as computed at $z = 0$ and $z = -H_{rms}$ and with horizontal axes proportional to a rough estimation of the uncertainty in the length scale evaluation. On observing the pictures of test Nos. 66 and 61 (Fig. 2 in the companion paper), it appears that the turbulence integral length scale Λ_{zz} is generally smaller than the length scale of the dominant surface features L , and that the plot points should be translated towards the right in the diagram. Obviously, the shapes of the coherent structures impinging the free surface are quite important, and a more detailed classification of surface deformation would require using multiple length scales and a consequent multi-parameter description. Note also that the relation between

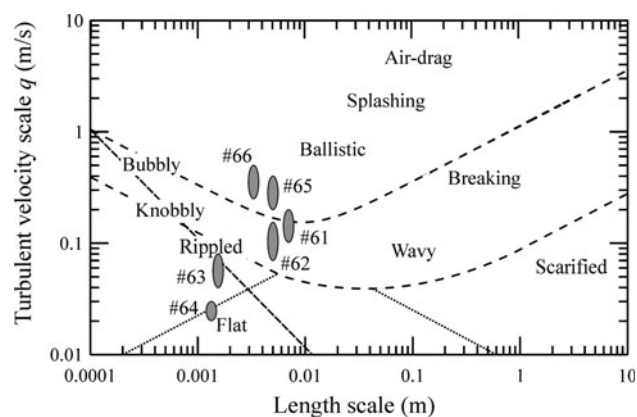


Fig. 16 Diagram of turbulence velocity scale and length scale of dominant surface features (Brocchini and Peregrine 2001). The ellipses represent the present experiments output

L and Λ_{zz} appears not to be monotonic: test No. 61 has the maximum integral length scale but apparently not the maximum length scale L .

3.3 The correlation between the free surface and fluid velocity

The coherence between the two variables a and b is defined as

$$\psi = \frac{P_{ab}^2}{P_{aa}P_{bb}} \tag{18}$$

where P_{ab} is the power cross-spectral density and P_{aa} and P_{bb} are the power autospectral densities; the coherence ranges between 0 and 1. The analysis of the correlation between the free surface and vertical velocity fluctuations is shown in Figs. 17 18, 19, 20. The upper boxes are the coherence maps for the vertical and streamwise velocity components, and the lower boxes are the phase lag maps, with positive values of the phase indicating that the free surface elevation has a delay with respect to the velocity fluctuations. Similar maps for the spanwise velocity component show a negligible coherence value and will not be considered further. In the present tests, the coherence generally has a maximum value immediately below the mean water level and at frequencies from 3.3 Hz to slightly less than 2 Hz for decreasing values of H_{rms} . The maximum coherence has a value less than ~ 0.3 and decreases with H_{rms} for all the tests.

The maximum lies at higher frequencies or near the main peak of the free surface elevation power spectrum.

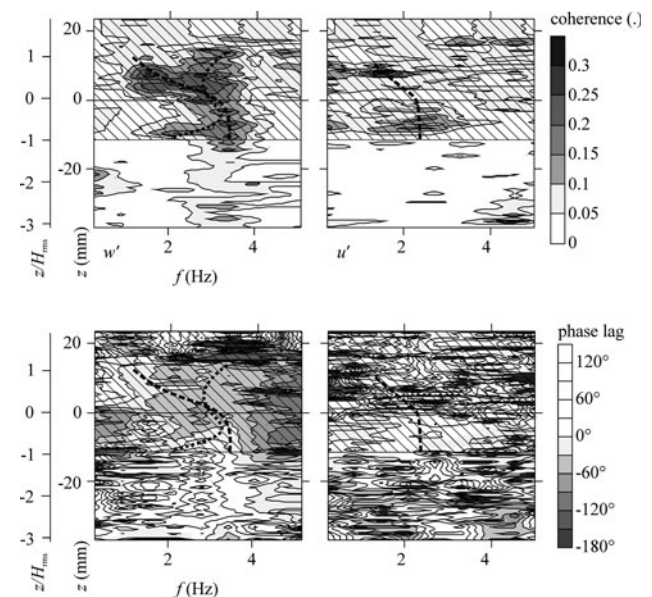


Fig. 17 Coherence and phase map between free surface level and fluctuating vertical velocity–streamwise velocity. Test $H_{rms} = 12.09$ mm (test No 66)

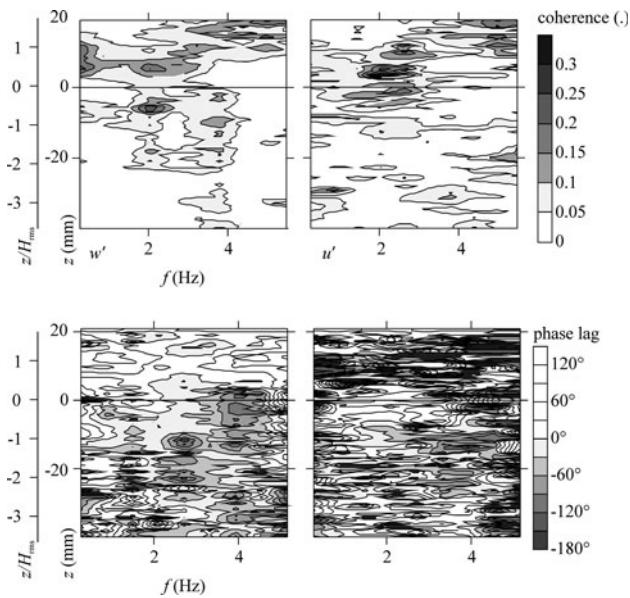


Fig. 18 Coherence and phase map between free surface level and fluctuating vertical velocity–streamwise velocity. Test $H_{rms} = 10.96$ mm (test No 65)

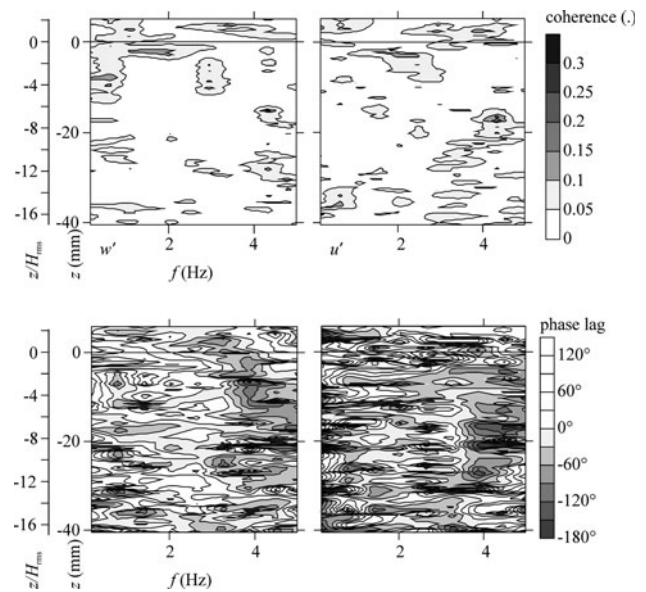


Fig. 20 Coherence and phase map between free surface level and fluctuating vertical velocity–streamwise velocity. Test $H_{rms} = 2.44$ mm (test No 62)

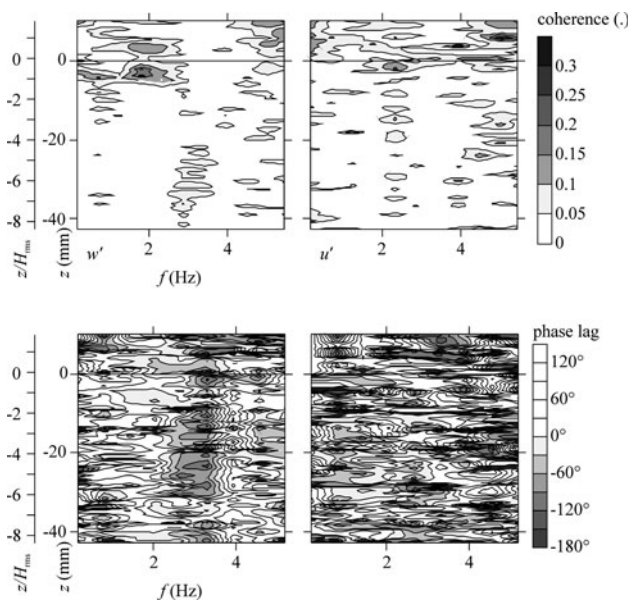


Fig. 19 Coherence and phase map between free surface level and fluctuating vertical velocity–streamwise velocity. Test $H_{rms} = 5.25$ mm (test No 61)

Occasionally, two peaks can be found, with the second at twice the main frequency. At a high value of H_{rms} (test No. 66), we can observe that the phase lag between the free surface fluctuations and the vertical velocity fluctuations is generally negative in the free surface layer, i.e. the free surface fluctuations are advanced with respect to the vertical velocity fluctuations; it happens that where the coherence is maximal, the phase lag changes from 0° to

-90° at the zero level, then increases again (see the dashed and the dotted thick curves in Fig. 16). The phase lag is positive below the free surface layer, i.e. the free surface fluctuations have a delay with respect to the vertical velocity fluctuations. In the same test, the phase lag between the free surface fluctuations and the streamwise velocity fluctuations is positive in the domain where the maximum coherence occurs. Note that while two separate curves connecting the maxima can be drawn for the vertical velocity fluctuations (ranging between 1 and 3.5 Hz), a single curve can be drawn for the streamwise velocity fluctuations (in the range 1–2 Hz). One way to interpret the data assumes that the streamwise velocity fluctuations act as a forcing term for the free surface fluctuations, with maximal efficiency near the observed peak of 2 Hz; the free surface fluctuations, in turn, force the vertical velocity fluctuations with maximal efficiency in two bands, one centred at 2 Hz and the second at almost twice the peak frequency of 2 Hz. The superharmonic of the response occurs because both the crests and the troughs excite the eddies and, hence, the velocity fluctuations. The mechanism of wave generation by turbulence in the water could be as described by Teixeira and Belcher (submitted), with a forcing dominated by turbulent pressure fluctuations. This scenario can also be recognised for test No. 65 and partially for the other tests at lower values of H_{rms} . The appearance of microbreakers should improve the generation of vertical velocity fluctuations.

Some preliminary results reported by Dabiri and Gharib (2001) show that at a very small free surface elevations (less than ± 1.2 mm), the near-surface deformation best

correlates with the normal vorticity. Using the present data, we cannot evaluate vorticity, but we find that at low values of H_{rms} the coherence between the free surface elevation and the vertical velocity is very low.

4 Conclusions

These results show the characteristics of free surface–turbulent flows at low, but not negligible, Froude numbers without air inception.

In the boundary layer, the turbulent kinetic energy is monotonic and is well fitted by an error function, with $u'_{\text{rms}} > v'_{\text{rms}} \gg w'_{\text{rms}}$. The redistribution ratios of the turbulent energy are almost uniform. The streamwise–vertical component of the Reynolds stress depends on the Froude number. At high Froude numbers, a net momentum influx towards the flow field is generated by the free surface–boundary layer. At a lower Froude number, the sign of the Reynolds stress is inverted. The process of stress transfer is controlled by the role played by the free surface fluctuations, which are essentially passive below a threshold, after which they become active. At different regimes, the free surface fluctuations correlate with the velocity fluctuations in a different way (mainly through vertical and streamwise velocity fluctuations).

Some more specific characteristics of macroturbulence are analysed using invariant analysis. At high Froude numbers, turbulence starts in a one-component manner near the free surface, becoming disc-like axisymmetric, with two larger streamwise and spanwise stresses. At small Froude numbers, the turbulence becomes two-component in the horizontal plane near the free surface, evolving towards disc-like axisymmetric beneath it. Also, the effects of the free surface waves are evident when the invariants are analysed separately below the crests and troughs. The auto-correlations for the vertical fluctuating velocity along the vertical direction are non-symmetric. The computed integral macroscale assumes a maximum value at an intermediate Froude number, presumably as a consequence of an optimal tuning between free surface oscillations and macrovortices. At low Froude numbers, the macroscale is damped near the mean water level, whereas at high Froude numbers, the macroscale is uniform in the vertical direction or it increases towards the mean water level. A similar behaviour is observed for the Taylor vertical length scale for the vertical velocity. The macroscale and the microscale are related through the Reynolds number (based on the integral length scale of the turbulence), but the microscales (dissipation scales) decrease much faster than they would under equilibrium conditions (dissipation = production). This phenomenon is particularly

evident in a test with optimal tuning between the turbulence and free surface elevation.

An analysis of the correlation between free surface instantaneous elevation and the vertical component of fluctuating velocity reveals that the free surface is generally delayed with respect to fluid velocity, except at high values of H_{rms} . We can infer that free surface fluctuations are generally triggered by turbulence, but strong fluctuations of the free surface can easily invert the roles. The triggering mechanism could be that inferred by Teixeira and Belcher (submitted), with pressure fluctuations related to turbulence and generating the free surface fluctuations.

Acknowledgments Support from FIL 2008 is acknowledged. The paper was completed and revised during my sabbatic leaving in CEAMA, Grupo de Dinámica de Flujos Ambientales, University of Granada, Spain, where I was kindly hosted by Miguel A. Losada.

References

- Battjes JA, Sakai T (1981) Velocity field in a steady breaker. *J Fluid Mech* 111:421–437
- Britter RE, Hunt JCR, Richards KJ (1981) Air flow over a two-dimensional hill: studies of velocity speed-up, roughness effects and turbulence. *Q J R Meteorol Soc* 107:91–110
- Brocchini M, Peregrine DH (2001) The dynamics of strong turbulence at free surfaces. Part 1. Description. *J Fluid Mech* 449:225–254
- Brumley BH, Jirka GH (1983) Near-surface turbulence in a grid-stirred tank. *J Fluid Mech* 183:235–263
- Calmet I, Magnaudet J (2003) Statistical structure of high-Reynolds-number turbulence close to the free surface of an open channel flow. *J Fluid Mech* 474:355–378
- Dankwerts PV (1951) Significance of liquid-film coefficients in gas absorption. *Ind Eng Chem* 43:1460
- Handler RA, Swann TF Jr, Leighton RI, Swearingen JD (1993) Length scales and the energy balance for turbulence near a free surface. *AIAA J* 31:1998–2007
- Higbie R (1935) The rate of absorption of a pure gas into a still liquid during short periods of exposure. *AICHe Trans* 31:365
- Komori S, Murakami Y, Ueda H (1989) The relationship between surface-renewal and bursting motions in an open-channel flow. *J Fluid Mech* 203:102–123
- Longo S (2010) Experiments on turbulence beneath a free surface in a stationary field generated by a Crump weir: free surface characteristics and the relevant scales. *Exp Fluids*. doi:10.1007/s00348-010-0881-5
- Lumley JL, Newman GR (1977) The return to isotropy of homogeneous turbulence. *J Fluid Mech* 82:161–178
- McCready MA, Vassiliadou E, Hanratty TJ (1986) Computer simulation of Turbulent mass transfer at a mobile interface. *AICHe J* 32:1108
- Nakagawa HI, Nezu I (1977) Predictions of the contributions to the Reynolds stress from the bursting events in open channel flows. *J Fluid Mech* 80:99–128
- Nezu I, Nakagawa HI (1993) Turbulence in open channel flows. *IAHR Monograph Series*, pp. 281 + xii, ISBN 9054101180
- Phillips OM (1957) On the generation of waves by turbulent wind. *J Fluid Mech* 2:417–445
- Shen L, Zhang X, Yue DKP, Triantafyllou GS (1999) The surface layer for free-surface turbulent flows. *J Fluid Mech* 386:167–212

- Simonsen AJ, Krostad P-Å (2005) Turbulent stress invariant analysis: clarification of existing terminology. *Phys Fluids* 17:088103
- Sirkar KK, Hanratty TJ (1970) Turbulent mass transfer rates to a wall for large Schmidt numbers to the velocity field. *J Fluid Mech* 44:598
- Swean TF, Leighton RI, Handler RA, Swearingen JD (1991) Turbulence modelling near the free surface in open channel flow. AIAA Paper 91-0613
- Tamburrino A, Gulliver JS (1999) Large flow structures in a turbulent open-channel flow. *J Hydraul Res* 37(3):363–380
- Tamburrino A, Gulliver JS (2002) Free-surface turbulence and mass transfer in a channel flow. *AIChE J* 48(12):2732–2743
- Teixeira MAC, Belcher SE (2002) On the distortion of turbulence by a progressive surface wave. *J Fluid Mech* 458:229–267
- Tennekes H, Lumley JL (1972) *A first course in turbulence*. The MIT Press, pp. 300 + xii, ISBN 0-262-20019-8
- Thais L, Magnaudet J (1996) Turbulent structure beneath surface gravity waves sheared by the wind. *J Fluid Mech* 328:313–344